nature communications

Article

https://doi.org/10.1038/s41467-024-51280-2

High vacancy formation energy boosts the stability of structurally ordered PtMg in hydrogen fuel cells

Received: 23 January 2024

Accepted: 31 July 2024

Published online: 15 August 2024

Check for updates

Caleb Gyan-Barimah[1], Jagannath Sai Pavan Mantha[2], Ha-Young Lee[3], Yi Wei[1], Cheol-Hwan Shin[1], Muhammad Irfansyah Maulana[1], Junki Kim[1], Graeme Henkelman[2] ✉ & Jong-Sung Yu[1,3] ✉

Alloys of platinum with alkaline earth metals promise to be active and highly stable for fuel cell applications, yet their synthesis in nanoparticles remains a challenge due to their high negative reduction potentials. Herein, we report a strategy that overcomes this challenge by preparing platinum-magnesium (PtMg) alloy nanoparticles in the solution phase. The PtMg nanoparticles exhibit a distinctive structure with a structurally ordered intermetallic core and a Pt-rich shell. The PtMg/C as a cathode catalyst in a hydrogen-oxygen fuel cell exhibits a mass activity of 0.50 A mg_{Pt}^{-1} at 0.9 V with a marginal decrease to 0.48 A mg_{Pt}^{-1} after 30,000 cycles, exceeding the US Department of Energy 2025 beginning-of-life and end-of-life mass activity targets, respectively. Theoretical studies show that the activity stems from a combination of ligand and strain effects between the intermetallic core and the Pt-rich shell, while the stability originates from the high vacancy formation energy of Mg in the alloy.

The oxygen reduction reaction (ORR) occurring at the cathode of the polymer electrolyte membrane fuel cell (PEMFC) to date requires precious metals; mainly platinum (Pt) for efficient catalysis[1,2]. However, the high cost, large dosage, relative instability, and extreme scarcity of Pt limit its use for practical applications[3–5]. Considering Sabatier's principle that an excellent ORR catalyst should exhibit intermediate binding strength for OH* (E_{OH})[6], various groups have resorted to methods of alloying platinum with early transition metals (Sc, Ti, V)[7,8], late transition metals (Ni, Co, Fe)[9–14], and rare earth metals (Y, La, Ce)[15–20]. Such alloy systems tend to lower the d-band center (E_d) of Pt which subsequently optimizes its binding with reaction intermediates[21]. Since the surface atoms of electrocatalysts predominantly participate in ORR, the core-shell nanostructure with a Pt-rich shell has been adopted as the most successful design. In these alloys, the ligand effect existing between the non-noble metal core and the Pt shell exerts a compressive strain on the Pt shell, which enhances the catalytic activity. However, there is still room for improvement for these catalysts in terms of overall Pt utilization and durability[22,23]. In this regard, alloys of Pt with earth-abundant alkaline earth metals (AEMs) such as calcium (Ca), strontium (Sr), and magnesium (Mg) are great alternatives to those of Pt with late transition metals[24–28]. This is because alloys of Pt with AEMs are expected to exhibit high negative heat of formation comparable to those of Pt with rare earth or early transition metals[29]. Such cohesive energy is postulated to prevent the subsurface migration of the secondary metal[28,30]. Among the AEMs, Mg is very cheap, abundant (13.1% by mass) and the fourth most common element on the earth after iron (32.1%), oxygen (30.1%), and silicon (15.1%), making it a promising alloying component for sustainable fuel cell electrocatalyst development[31]. AEMs, besides their abundance and low cost, when alloyed with Pt tend to form intermetallic compounds which are known to be very stable in solution[24,32,33]. Furthermore, when such atomic ordering occurs, the alloys derive unique properties that differ significantly from those of their isolated elements. Escudero-Escribano et al.[34] report that AEMs are relatively unstable in acidic electrolytes, and hence, in their alloyed states, the secondary metal at the edges of the particles dissolves in solution, leaving behind a Pt-rich

[1]Department of Energy Science and Engineering, Daegu Gyeongbuk Institute of Science & Technology (DGIST), Daegu, Republic of Korea. [2]Department of Chemistry, The University of Texas at Austin, Austin, TX, USA. [3]Energy Science and Engineering Research Center, DGIST, Daegu, Republic of Korea. ✉e-mail: henkelman@utexas.edu; jsyu@dgist.ac.kr

skin[34]. This phenomenon as explained from theoretical calculations reveals that the surface Pt-Pt bond distance shortens[35], which leads to the weakening of the interaction between surface Pt and reaction intermediates such as O*, OH*, and OOH*[36,37]. Despite the unique properties these alloys provide, their synthesis in nanoparticulate form remains tricky owing to their high negative standard reduction potentials (−2.37 V vs SHE for Mg^{2+}//Mg) compared to that of Pt (+1.20 V vs SHE).

Over the years, many strategies such as the top-down approach (gas condensation, spray pyrolysis, and ball milling) have been used to synthesize nanomaterials for various catalytic applications[38,39]. In 2020, Yu's group through this top-down approach reported the first PtMg nanoparticles (NPs) by mixing metallic Mg powder with Pt NPs anchored on a carbon support, followed by annealing in an H_2/Ar atmosphere at 650 °C[28]. Ever since this report, significant attention has been drawn to this class of materials. However, the top-down approach presents bottlenecks; the main one being the lack of control over the structures in terms of morphology and uniform distribution of elements. Additionally, the top-down approach adopted by Yu's group requires alloying at a minimum temperature corresponding to the melting point of the secondary metal, making it tedious to obtain Pt-alloys with metals that have very high melting points. Various methods such as the hydrogenation of Li_2MgPt[40], reacting solid metals with magnesium hydride[41], and the melting of metal ingots[42], have resulted in PtMg alloys with different crystal structures, yet, the small surface-to-volume ratios make them unsuitable for nanostructured applications. In contrast to the physical methods, the bottom-up (chemical method) approach represents the most promising way of having precise control over structures for NPs. This is usually achieved by the reduction or thermal decomposition of metal precursors at low temperatures with the help of organic ligands or surfactants and solvents followed by reductive annealing at high temperatures. With this background, in this work, our group reports a Pt-AEM alloy synthesized through the solution phase approach. In solution, AEMs are extremely oxyphilic with very high negative reduction potentials (Mg//Mg^{2+}; −2.370 V, Ca//Ca^{2+}; −2.870 V, Sr//Sr^{2+}; −2.890 V, Ba//Ba^{2+}; −2.900 V). To alloy or dope them with Pt without significantly forming metallic oxides, the reduction of their precursors should be conducted by employing very fast reducing agents such as metal naphthalides or organoborohydrides and a non-aqueous aprotic solvent[8,31]. Protic aqueous solvents are not employed since the reduction potentials of AEMs are far beyond the stability range of water[43]. Furthermore, to obtain alloys of Pt with AEMs with precise control over structures, robust protectors must be employed since these alloys are prepared at high annealing temperatures. Researchers have employed different protective agents such as metal oxides, polymers, and molten KCl and NaCl matrices[8,44–47]. However, most of these protectors must be removed after the chemical synthesis since they tend to block the active sites of catalysts. Methods for the removal of these protectors are usually expensive and very tedious for most researchers, and hence, low and cost-efficient methods against NP growth and aggregation must be employed[48].

Herein, we report highly ordered PtMg alloys prepared through the solution phase with varying precursor composition of Pt to Mg; PtMg alloys with 1:1 and 3:1 Pt to Mg precursor mass ratios are herein denoted as PtMg/C-11 and PtMg/C-31, respectively. In all, the as-prepared NPs are relatively small with an average particle size distribution of 5.76 nm. Significantly, the PtMg/C-31 sample as a cathode catalyst in PEMFC exhibits a beginning-of-life (BOL) mass activity of 0.50 A mg_{Pt}^{-1}, which decreases to 0.48 A mg_{Pt}^{-1} after 30,000 electrochemical test cycles performed according to the US Department of Energy (DOE) protocol. This performance exceeds the DOE 2025 BOL and end-of-life (EOL) targets, demonstrating virtually no loss in activity for the PtMg catalyst during the 30k accelerated durability test (ADT) for electrocatalysts.

Results

Catalyst design and structural characterization

PtMg/C samples were prepared through three systematic steps namely; (I) solvolysis, (II) alloying and atomic ordering, and (III) creation of Pt-rich skin. The three-step synthesis route is illustrated schematically in Fig. 1a. Briefly, platinum (IV) chloride ($PtCl_4$), magnesium chloride ($MgCl_2$), sodium borohydride ($NaBH_4$), and N, N-dimethylformamide (DMF) were employed as the Pt and Mg precursors, the reducing agent, and the non-aprotic solvent, respectively. DMF is a non-aqueous aprotic solvent featuring a lower boiling point (153 °C) than most aprotic solvents available which can facilitate a faster collision between the Pt and Mg nuclei at a lower temperature. In addition, the polar nature of this solvent helps to solvate the metal chlorides. In the solvolysis step (I), all precursors aforementioned were weighed out as specified in the methods section in an argon-filled glove box, sonicated, and transferred into a Teflon-lined autoclave. Subsequently, the mixture was heated at 165 °C, which is above the boiling point of the solvent to increase the kinetic energy of the two metal nuclei for efficient collision. In the alloying and atomic ordering step (II), the obtained precipitate from the hydrothermal reaction of the initial precursors, solvent, and reducing agent at 165 °C was subjected to further reductive annealing in the presence of the fast-reducing agent; powdered potassium triethylborohydride (KEt_3BH) at 760 °C in 5% H_2/Ar atmosphere to obtain a structurally ordered intermetallic PtMg alloy (Fig. 1c, e). Before the Ar/H_2 treatment, the furnace was purged with ammonia (NH_3) until 180 °C since it provides a better protective atmosphere in the initial heating stage in comparison to the Ar/H_2 atmosphere[49]. KEt_3BH is very essential in the second reductive annealing step for the alloy formation, since the absence of this reagent results in a spectrum highly dominated by crystalline Pt and magnesium oxide (MgO) phases (Supplementary Fig. 1). Finally, in step III, the structurally ordered alloy was acid-etched in 0.5 M acetic acid to remove surface oxides and unreacted metal precursors (full details are in the methods section) and to create a Pt-rich skin (Fig. 1f). We then characterized the as-prepared samples using transmission electron microscopy (TEM), X-ray photoelectron spectroscopy (XPS), X-ray absorption spectroscopy (XAS) and powder X-Ray diffraction (PXRD). Further insights on the evolution of the alloy, composition, and temperature effects are discussed in the mechanistic study section.

PtMg alloys with different precursor ratios of Pt to Mg by mass were synthesized to test the effect of composition on the structure and catalytic property. Based upon our experience with the synthesis of AEM alloys, we started with a Pt to Mg precursor mass ratio of 3:1 and 1:1, herein denoted as PtMg/C-31 and PtMg/C-11, respectively. Inductively coupled plasma-optical emission spectrometry (ICP-OES) analysis shows that the PtMg/C-11 and PtMg/C-31 have Pt to Mg atomic ratios of 65.1:34.9 and 71.0:29.0, respectively.

The TEM image of PtMg/C-31 presented in Fig. 1b shows that the particles are uniformly distributed on the carbon substrate with a particle size ranging from 5 to 12 nm. The wide particle size range is attributed to the formation of two main intermetallic phases. In Fig. 1c, the high-angle annular dark-field scanning TEM (HAADF-STEM) image shows that some particles exhibit the $L1_0$ intermetallic structure (Fig. 1d) as evidenced by the alternating rows of Pt and Mg atoms, where the Pt atoms are in bright contrast to the dark Mg atoms owing to the difference in atomic numbers, while others show the $L1_2$ intermetallic structure (Supplementary Fig. 2). A critical study of the $L1_2$-ordered HAADF-STEM image in Supplementary Fig. 2b and the corresponding Fourier transformation (FFT) pattern (inset) shows that the particle is highly crystalline as revealed by the individually isolated reciprocal lattice diffraction spots. Furthermore, the presence of the (100) superlattice spot is consistent with the ordered nature of the PtMg/C-31 alloy. The d-spacings of 0.368 and 0.157 nm correspond to the (100) and (211) planes of Pt_3Mg, respectively. In comparison, the literature-recorded values for the $d_{Pt\text{-}Pt}$ in disordered (A1) Pt are 0.381

https://doi.org/10.1038/s41467-024-51280-2

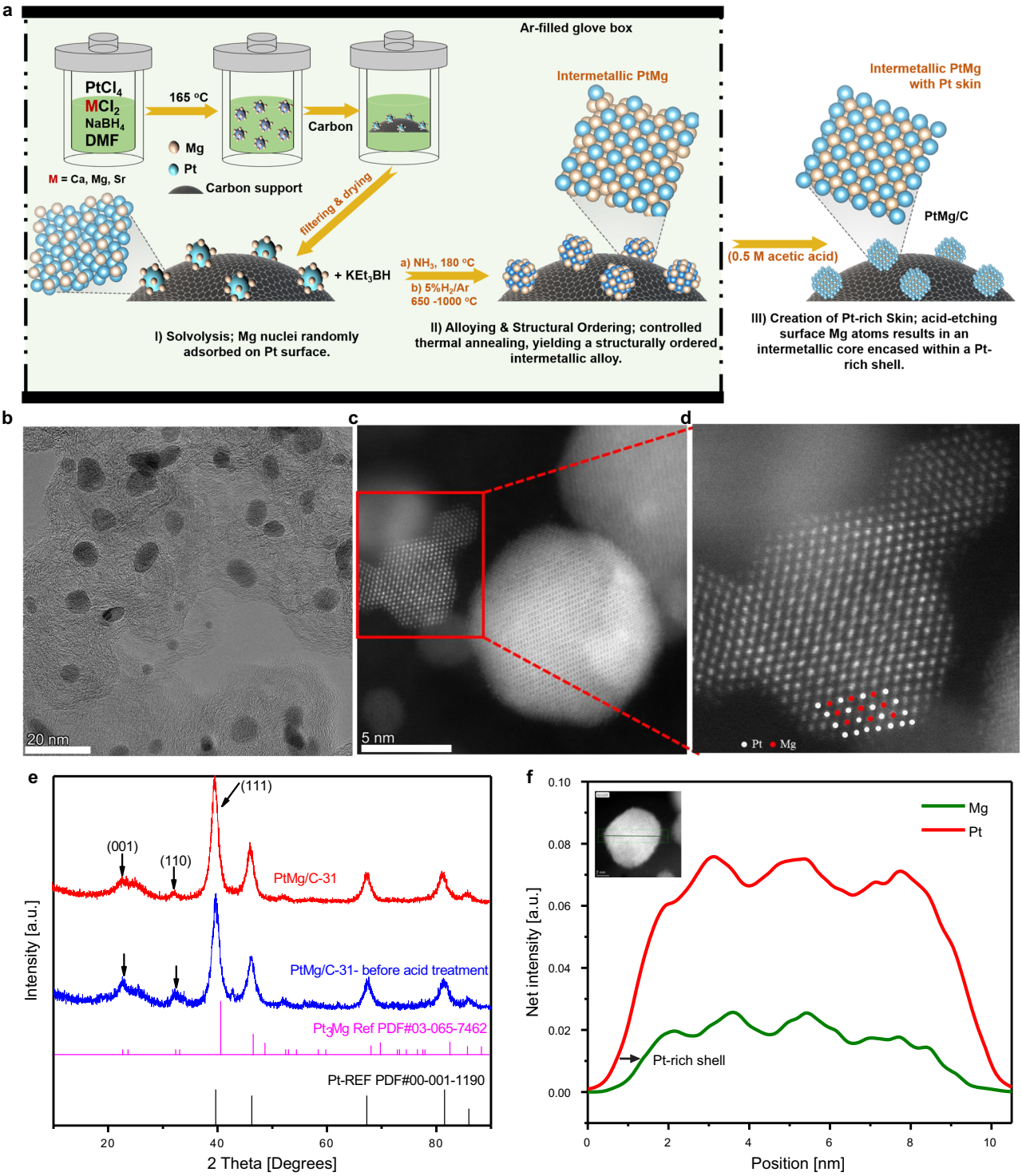

Fig. 1 | Synthesis and structural characterization. a Schematic representation of the synthesis of PtMg/C NPs **b** TEM image of the as-synthesized PtMg/C-31 NPs showing uniform distribution with little agglomeration. **c** HAADF-STEM image and **d** high-resolution image of the red-marked particle showing the orderly arrangement of the Pt (bright spots) and Mg (dark spots) atoms. **e** PXRD patterns of PtMg/C-31 before (blue) and after (red) acid treatment. **f** STEM-EDS line scan of a single PtMg/C-31 NP.

and 0.158 nm for the (100) and (211) planes, respectively. This shows that the introduction of Mg atoms introduces compressive strains along the <100> and <211> directions. Such compressive strains enhance the stability of the alloy in electrochemical conditions and reduce its adsorption strength with reaction intermediates[50,51]. The ordered structure is verified by the PXRD patterns presented in Fig. 1e as evidenced by the appearance of the (001) and (110) superlattice peaks. The XRD obtained conforms with the standard diffraction peak of Pt_3Mg (PDF#03-065-7462). STEM-EDS line scan (Fig. 1f) of a single particle confirms that the Pt and Mg are homogeneously distributed in the particle with a ~1 nm Pt-rich shell. All the conditions employed for the synthesis of PtMg/C-31 were maintained for PtMg/C-11 except for the varying Pt to Mg precursor mass ratio. A detailed study of the TEM, HAADF-STEM, and the corresponding EDS elemental mapping images

https://doi.org/10.1038/s41467-024-51280-2

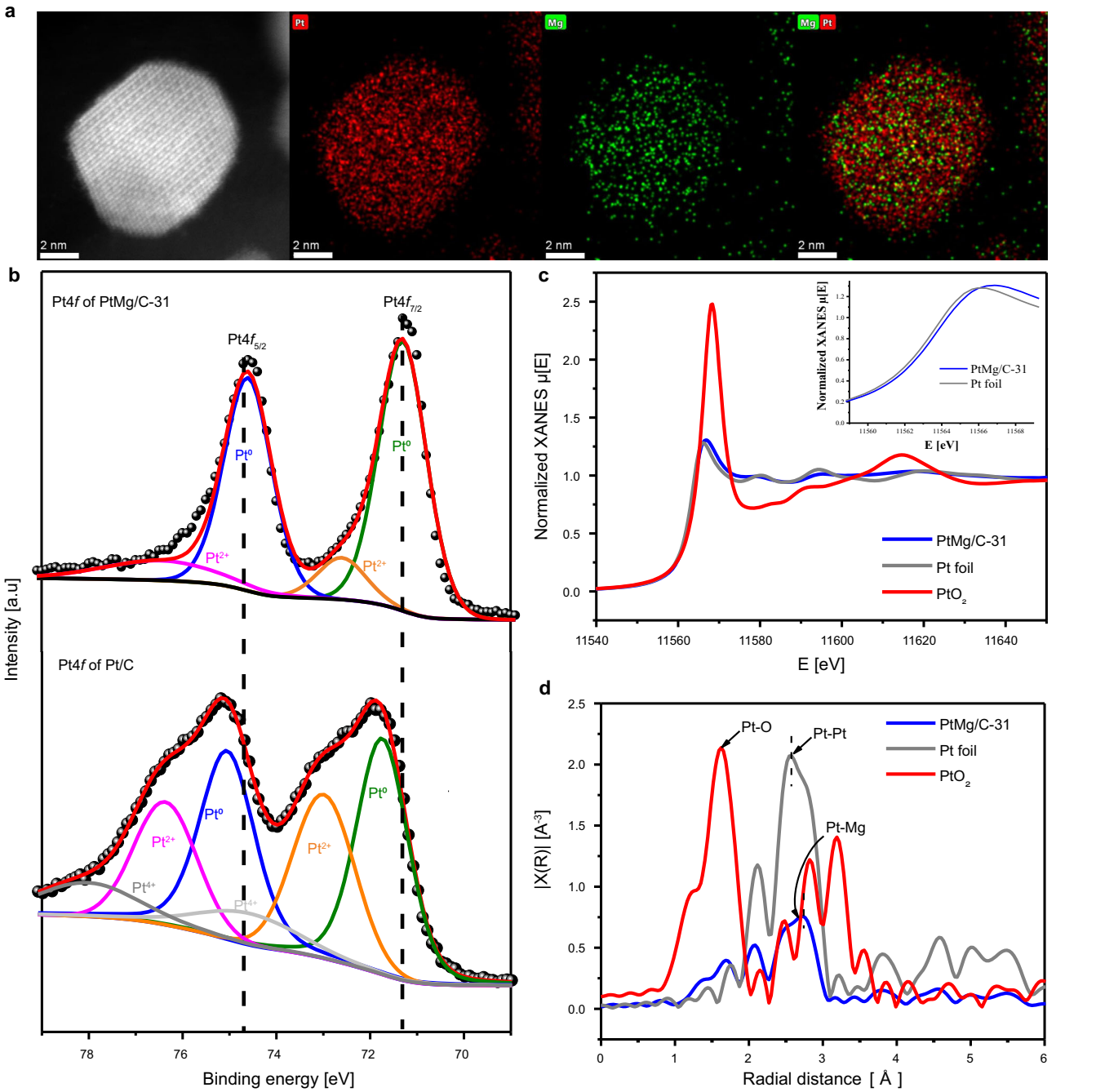

Fig. 2 | Elemental composition and oxidation state. a HAADF-STEM image and the corresponding EDS elemental mapping of a single structurally ordered PtMg/C-31 NP, showing Pt signal (red), Mg signal (green), and the overlapped signal. **b** High-resolution Pt 4*f* XPS profiles of PtMg/C-31 and commercial Pt/C. **c** Pt L_3 XANES and **d** Pt L_3 K^2 − weighted EXAFS spectra of PtMg/C-31, Pt foil, and PtO_2.

of the PtMg/C-11 in Supplementary Figs. 3 and 4 show a similar particle size distribution to that of the PtMg/C-31. Interestingly, HAADF-STEM images and EDS elemental mapping images illustrated in Supplementary Fig. 5, show that the PtMg/C-11 also exhibits a Pt-rich shell as well as the $L1_2$ and $L1_0$ intermetallic structures. Both of the aforementioned catalysts show interesting electrochemical performances and hence are discussed in detail in the electrochemical section.

The elemental distribution and oxidation states of PtMg/C-31 were studied through energy-dispersive X-ray spectroscopy (EDS) and XPS analyses. In Supplementary Figs. 6 and 7, the STEM images and the corresponding EDS elemental mapping images show that Pt and Mg are homogeneously distributed throughout the particles. This confirms the alloy formation since the Mg or any of its derivative compounds would have been washed out during the 12-hour acid-etching process. Furthermore, the STEM and the corresponding EDS elemental mapping images in Fig. 2a show that the area corresponding to the Pt signal is slightly larger than that of Mg, indicating the formation of a Pt-rich shell. The STEM image in Supplementary Fig. 2a (yellow arrows) supports the result with about 1∽3 layers of Pt observed in the outmost surface. Due to the difference in atomic radii of Pt and Mg (139 and 160 nm, respectively) and the large difference in electronegativity, the electronic structures of both Pt and Mg are expected to be modified owing to the ligand and strain effects. We used XPS analysis to explore the impact of Mg on the surface chemical state of the as-synthesized PtMg/C-31 alloy. High-resolution Pt 4*f* doublets were observed for both the PtMg/C-31 and commercial Pt/C.

https://doi.org/10.1038/s41467-024-51280-2

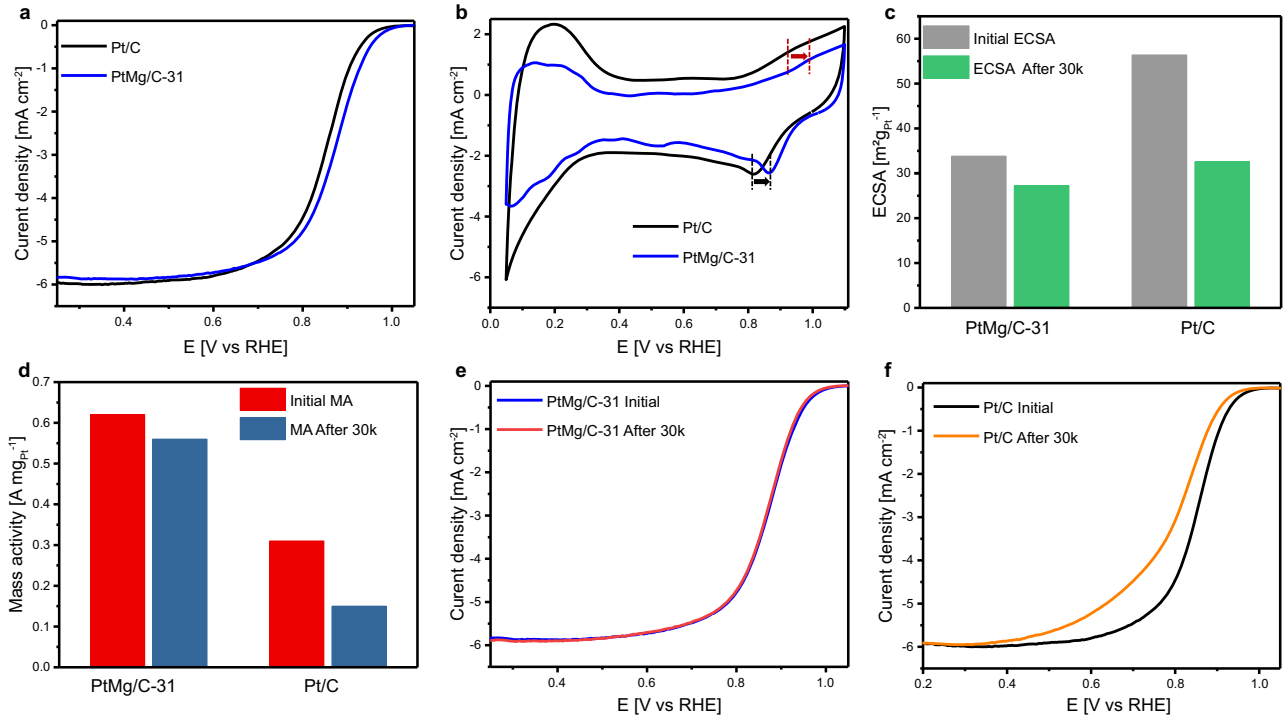

Fig. 3 | Liquid half-cell tests. a Linear sweep voltammetry (LSV) curves, **b** cyclic voltammograms (CVs) for PtMg/C-31 and commercial Pt/C recorded in O_2-saturated solution. **c** Electrochemically active surface areas (ECSAs) and **d** mass activities determined at 0.9 V for PtMg/C-31 and commercial Pt/C before and after 30,000 accelerated durability tests (ADT). LSVs recorded before and after the ADT **e** for PtMg/C-31 and **f** for Pt/C. Note: All electrochemical measurements were conducted in a 0.1 M $HClO_4$ solution at room temperature. The durability tests were performed according to the DOE protocol described in the Supplementary Information.

Binding energies of 71.40 and 71.74 eV are determined for the Pt4$f_{7/2}$ of PtMg/C-31 and Pt/C, respectively (Fig. 2b). The negative shift observed in the PtMg/C-31 doublet relative to commercial Pt/C is associated with the strain and the ligand effects existing between Pt and Mg[4,52–54]. The large shift may also be attributed to a significant amount of Pt oxides existing at the surface of the Pt NPs. The alloy formation between Pt and Mg prevents such a significant degree of oxidation. A similar shift is observed in the PtMg/C-11 (Supplementary Fig. 8). Furthermore, to show the existence of metallic Mg (Mg^0), we deconvoluted the high-resolution Mg 1*s* spectrum (Supplementary Fig. 9). Integration of the areas under the two main doublets at binding energies of 1303.7 and 1304.9 eV for Mg^0 and Mg^{2+}, respectively shows that metallic Mg dominates over the +2-oxidation state.

X-ray absorption spectroscopy (XAS) was conducted to understand the coordination environment and the valence state in Pt foil, PtO_2, and PtMg/C-31. X-ray absorption near edge structure (XANES) spectra and the insert (Fig. 2c) show that the absorption edge of PtMg/C-31 is located between those of the Pt-foil and PtO_2 but is much closer to the Pt foil. This suggests that the oxidation state of Pt in the PtMg/C-31 is close to the metallic state. The white line peak intensity, which is associated with the transition of an electron from the core 2*p* 3/2 orbital to the unoccupied 5*d* orbitals of the Pt L_3 edge is large for PtO_2 but shows almost similar low intensity for Pt foil and PtMg/C-31, suggesting a low degree of catalyst oxidation. Fourier transform of the higher energy regions gives rise to extended X-ray absorption fine structure (EXAFS) spectra which provide information about the coordination environment of the Pt atoms. The fitting results provided in Supplementary Fig. 10 and Supplementary Table 1 show that the Pt-Pt bond distance in PtMg/C-31 (2.75 Å) is shorter than in the Pt foil (2.76 Å). This indicates that in the first coordination shell, the Pt-Pt bonds are compressively strained as a result of alloying with Mg. The EXAFS results shown in Fig. 2d also show the presence of a Pt-Mg bond with a bond length of (2.763 Å). It must be emphasized that the bond lengths of Pt-Pt and Pt-Mg in the first coordination shell are similar.

Electrochemical half-cell evaluation

The electrochemical sensitivity and reactivity of our as-synthesized catalysts towards oxygen reduction reaction (ORR) were determined by cycling the PtMg/C electrocatalysts deposited on glassy carbon with an active area of 0.071 cm^2 in an N_2 or O_2-saturated 0.1 M $HClO_4$ electrolyte. The rotating disk electrode (RDE) cell configuration consisted of glassy carbon coated with either the as-synthesized catalyst or commercial Pt/C as the working electrode, with a Pt wire as the counter electrode and Ag/AgCl as the reference electrode (details are provided in the supplementary information)[55]. The metal weight percent as determined on the carbon support was 16.0 and 19.4 wt%, respectively for PtMg/C-31 and Pt/C (Supplementary Fig. 11) according to thermogravimetric analysis (TGA) data.

First, we tested the electrocatalytic performance of PtMg/C-31, and the performance showed a half-wave potential ($E_{1/2}$) of 0.87 V vs RHE, which is superior to commercial Pt/C with an $E_{1/2}$ of 0.84 V vs RHE as evidenced by the positively shifted onset potential and LSV curve (Fig. 3a). Furthermore, the CVs presented in Fig. 3b show a positive shift to higher potential of the Pt-oxide formation peak (red arrow) for the PtMg/C-31 as compared to Pt/C. This signifies that the PtMg/C-31 is less likely to suffer from catalyst oxidation, which would retard its dissolution and subsequently decrease Ostwald ripening. In addition, the oxygen reduction peaks in the potential region of 0.7 to 0.9 V vs RHE (black arrow) show a similar positive shift, suggesting that the interaction between Pt and the oxygen intermediates in the PtMg/C-31 is weaker than that of the Pt/C. Per Sabatier's principle, a catalyst with too strong binding may lead to difficulty in desorption, hence, resulting in the lower electrocatalytic performance observed for the commercial Pt/C. Further information obtained from the CV curves

shows that the hydrogen adsorption and desorption regions that characterize the electrochemically active surface areas for Pt-based catalysts were smaller for PtMg/C-31 than Pt/C with values of 33 and 56 m^2g^{-1}, respectively (Fig. 3c). Despite the lower ECSA of PtMg/C-31, the enhanced activity is thought to originate from the strain and ligands effects of the Mg on the Pt rather than the particle size effect. Similar trends have also been observed in other alloys[51].

The accelerated durability test (ADT) was evaluated in a N_2-saturated 0.1 M $HClO_4$ within the potential range from 0.60 and 0.95 V vs RHE at a scan rate of 100 mV s^{-1} for 30,000 potential cycles according to the DOE protocol[56]. In Fig. 3d, the BOL mass activity (MA) initially recorded for PtMg/C-31 was 0.62 A mg_{Pt}^{-1}, with EOL mass activity of 0.56 A mg_{Pt}^{-1} after 30,000 cycles (only 10% degradation). In contrast, commercial Pt/C shows BOL and EOL mass activities of 0.31 and 0.15 A mg_{Pt}^{-1}, respectively. In full agreement with the above results, the improved stability of PtMg/C-31 is visualized in Fig. 3e, where the LSV curves before and after 30,000 ADT cycles almost overlap while that of the commercial Pt/C decreases significantly with a half-wave potential loss of 0.35 mV (Fig. 3f). The specific activity (SA) was evaluated by normalizing the mass activities with their corresponding ECSAs. The specific activities for PtMg/C-31 and Pt/C at the BOL were 1.8 and 0.55 mA cm^{-2} respectively. This indicates efficient utilization of the PtMg/C-31 ECSA (Supplementary Fig. 12a). In addition, the CVs recorded before and after the 30,000 ADT overlapped with only a small change in the hydrogen desorption area (Supplementary Fig. 12b). The resulting ECSA presented in Fig. 3c shows a 19% drop for PtMg/C-31 while a more significant loss of 42% was recorded for Pt/C. These half-cell data demonstrate the high durability of PtMg/C-31 for ORR.

We also tested the electrocatalytic performance of the PtMg/C-11, and the performance was good as both the onset and half-wave potentials are shifted to more positive potentials relative to the reference Pt/C (Supplementary Fig. 13a). The ADT results conducted for the PtMg/C-11 show that there is only a small change in the onset potentials of the LSVs but the half-wave potential before and after the 30k ADT cycles is maintained (Supplementary Fig. 13c). A loss in ECSA similar to that recorded for the PtMg/C-31 can be observed in Supplementary Fig. 13d.

Mechanistic study

To explain the origin of these results, we took a step-by-step approach to explore the effect of composition and heating temperature on the formation of the PtMg alloys. First, we studied the effect of the composition on the degree of ordering. When all the synthesis conditions reported in the methods section were maintained except for varying the precursor composition of Pt to Mg, it can be realized from Supplementary Fig. 14 that the degree of ordering increases with increasing amounts of Mg. This is evidenced by the appearance and intensification of the (110) and (001) peaks as we move from PtMg/C-31, PtMg/C-11 to PtMg/C-13 (Pt: Mg precursor mass ratio of 1:3). The corresponding TEM images presented in Supplementary Fig. 15 show that all the PtMg alloy NPs are evenly distributed on the carbon substrate. The average particle size distribution is 5.81 and 5.76 nm for PtMg/C-11 and PtMg/C-31, respectively. In contrast, the TEM image of PtMg/C-13 (Supplementary Fig. 15c) reveals the presence of highly aggregated particles, as corroborated by sharp peak intensities observed in the PXRD patterns (Supplementary Fig. 14). ICP-OES analysis indicates that PtMg/C-13 exhibits a Pt:Mg atomic ratio of 63.4:36.6. These findings suggest that, at the optimal temperature of 760 °C, varying the initial Mg content does not significantly influence the composition of the nanoparticles; rather, it primarily affects the degree of ordering as seen in Supplementary Fig. 14. This phenomenon explains the marginal differences observed in the atomic ratios.

Similarly, the effect of temperature on the PtMg/C-31 was also studied by maintaining all other conditions specified in the methods section (Supplementary Fig. 16). XRD patterns obtained after the first reduction process at 165 °C conform with that of crystalline Pt. This suggests that the Mg reacts with the Pt in some way, and otherwise, the Mg would have been lost during washing. The absence of additional peaks corresponding to $MgCl_2$ or other Mg moieties such as MgO or $Mg(OH)_2$ further supports this postulation. When the temperature was raised in the annealing process, the results presented in the same figure show that the crystalline Pt phase remains dominant at temperatures as high as 600 °C. However, when the temperature was increased to 650 °C, the structurally ordered PtMg alloy was observed as evidenced by the appearance of the (110) superlattice peak. Increasing the temperature from 650 to 800 °C resulted in the appearance of the (001) diffraction peaks and an increase in the intensity of the (110) superlattice peaks. Among all the samples prepared at the different annealing temperatures, the sample obtained at 760 °C showed the best catalytic performance. Hence, all control samples were also synthesized at the same temperature. The resulting TEM images and particle size distributions of the temperature-variant samples are presented in Supplementary Fig. 17. In short, we found the formation of the PtMg alloy to be influenced by temperature and composition. Increasing the Pt to Mg ratio beyond a certain threshold value (for example, a sample with Pt to Mg precursor mass ratio of 3:0.5) could limit the alloy formation as indicated in Supplementary Fig. 18, resulting in poor catalytic performance. The optimum Pt to Mg mass ratio was determined to be 3:1.

Membrane electrode assembly (MEA) full cell evaluation

The performance obtained from half-cell RDE test with PtMg/C samples prompted us to evaluate the performance in a practical fuel cell by employing each of the two electrocatalysts (PtMg/C-31 and PtMg/C-11) as the cathode of the MEA under H_2-O_2/air conditions. Under the same test conditions, the commercial Pt/C (19.4 wt% Tanaka, Japan) was used as a reference catalyst for efficient comparison. All polarization curves presented in this section were determined under iR-free conditions. The polarization curves obtained at 80 °C under the H_2-O_2 gas flow in Supplementary Fig. 19a show that the PtMg/C-31 exhibits higher operating voltages for the same current densities. The initial power density documented for the PtMg/C-31 (1575 mW cm^{-2}) is higher than that of the commercial Pt/C (1465 mW cm^{-2}). Similarly, the performance of PtMg/C-31 and Pt/C was evaluated under H_2.air conditions in Supplementary Fig. 20. The initial peak power density recorded for both samples followed a comparable trend as those measured under H_2-O_2 conditions with values of 850 and 660 mW cm^{-2} for PtMg/C-31, and Pt/C respectively. Detailed values of the measurements are reported in Supplementary Table 2.

The stability of the electrocatalysts was determined by the potential-dependent cycling on the MEA between 0.60 and 0.95 V for 30,000 cycles according to the DOE accelerated durability test (ADT) protocol. Typical in the H_2-O_2 condition, the current density @ 0.8 V only dropped by 31 mA cm^{-2} (from 476 to 445 mA cm^{-2}) with a 6.5% loss for the PtMg/C-31 cathode. In contrast, at the same voltage, the Pt/C shows a ~ 49% loss in current density from 287 to 147 mA cm^{-2} (Supplementary Fig. 19b). The polarization curves recorded in Fig. 4a, b and the histogram of the peak power densities in Fig. 4h show that PtMg/C-31 is stable with only a 6% drop (1575 to 1480 mW cm^{-2}) after 30,000 ADT cycles, while the Pt/C exhibits a 30% loss (1465 to 1030 mW cm^{-2}) for the same number of cycles. Interestingly, the peak power density for the PtMg/C-31 at its EOL is higher than that of Pt/C at its BOL (Fig. 4h). In terms of overall Pt usage, the PtMg/C-31 reaches a BOL mass activity of 0.50 A mg_{Pt}^{-1} and EOL mass activity of 0.48 A mg_{Pt}^{-1} at 0.9 V, corresponding to only a 3% decrease after the 30,000 ADT cycles, surpassing the DOE 2020-2025 targets in terms of BOL and EOL mass activities (0.44 and 0.26 A mg_{Pt}^{-1} respectively). This performance overwhelms that of the Pt/C catalyst which shows a 49.6% loss in initial mass activity (from 0.22 A mg_{Pt}^{-1} (BOL) to 0.11 A mg_{Pt}^{-1} (EOL)), a performance well below the DOE targets (Fig. 4g).

https://doi.org/10.1038/s41467-024-51280-2

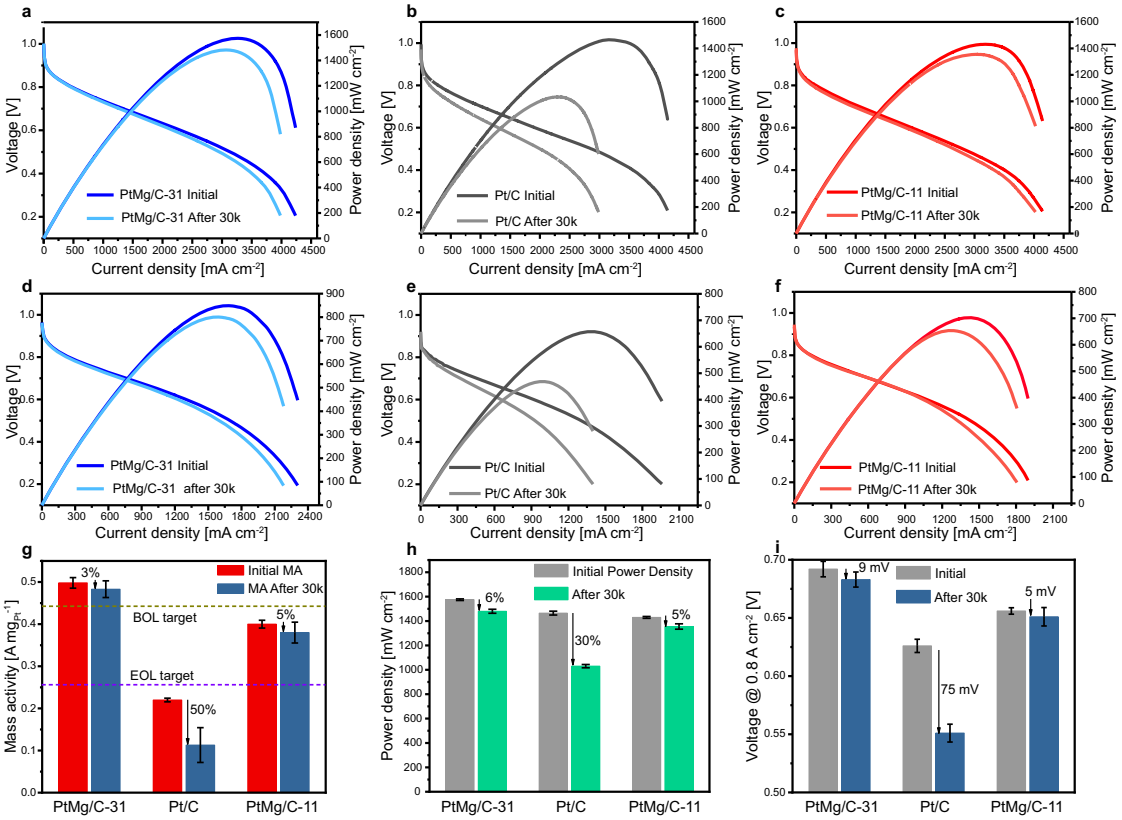

Fig. 4 | Fuel cell performance and durability tests. Polarization and power density curves before and after 30,000 cycles for **a** PtMg/C-31, **b** Pt/C, and **c** PtMg/C-11 in H_2-O_2 condition. Polarization and power density curves before and after 30,000 cycles for **d** PtMg/C-31, **e** Pt/C, and **f** PtMg/C-11 in H_2-air condition. Histograms of **g** mass activities, **h** peak power densities of PtMg/C-31, Pt/C, and PtMg/C-11 before and after 30,000 ADT cycles in H_2-O_2 gas flow, and **i** cell voltages recorded at 0.8 A cm^{-2} in H_2-air for the three catalysts before and after the 30,000 ADT (DOE Target <30 mV drop after ADT). Note: Detailed measurement conditions are indicated in the methods section. Error bars indicate the standard deviation for three independent measurements.

The stability test performed under the H_2-Air conditions (Fig. 4d, e) exhibited similar degradation patterns to those measured under H_2-O_2 as evidenced by the 6% drop in peak power density for PtMg/C-31 (850 to 800 mW cm^{-2}) and 29% for commercial Pt/C (660 to 470 mW cm^{-2}) (Supplementary Fig. 20b). The voltage drop at 0.8 A cm^{-2} was 9 and 75 mV for PtMg/C-31 and Pt/C, respectively in the H_2-air condition. (Fig. 4i). This voltage drop for PtMg/C-31 satisfies the DOE target of <30 mV drop after 30,000 ADT cycles. Interestingly, in contrast to numerous articles that report that the RDE tests are significantly different from the PEMFC tests, here, we show that similar performances reported in the half-cell tests are successfully repeated in the full-cell MEAs. In particular, the CVs recorded before and after the 30,000 stability test cycles in both the half-cell (Supplementary Fig. 12b) and full-cell (Supplementary Fig. 21) show similar degradation patterns despite the higher loss in ESCA observed in the hydrogen desorption region of the full cell MEA measurement.

Due to the similar activities of PtMg/C-31 and PtMg/C-11 recorded in liquid half-cell tests, we evaluated the PEMFC performance of the PtMg/C-11 under the same conditions. The polarization curves recorded in the H_2-O_2 condition in Fig. 4c show that the PtMg/C-11 exhibits similar performance to the commercial Pt/C sample in the high current density region, with a peak power density of 1430 mW cm^{-2}. However, interestingly, the kinetics of this sample in the low current density region was much improved as shown by the BOL mass activity of 0.40 A mg_{Pt}^{-1} (Fig. 4g). This sample also displayed stability similar to that observed for the PtMg/C-31 sample. The power density dropped by only 5% (from 1430 to 1355 mW cm^{-2}), while almost the same percentage drop was also recorded from the BOL to the EOL mass activity (0.38 A mg_{Pt}^{-1}). The corresponding measurement under H_2-air conditions is presented in Fig. 4f. This result is in contrast to that recorded in H_2-O_2 conditions as evidenced by the higher power density of 700 mW cm^{-2} compared to that of Pt/C with 660 mW cm^{-2}. These results emphasize the stability derived by alloying Pt with Mg. Supplementary Fig. 22 illustrates the H_2-O_2 fuel cell polarization and power density curves of the two PtMg/C samples and Pt/C recorded before the durability test. We postulate that the introduction of Mg atoms stabilizes the Pt atoms since both the stability and activity in the PtMg/C samples were higher than commercial Pt/C.

It is also worth noting that despite the similar electrocatalyst preparation method, the performance of PtMg/C-31 was higher than PtMg/C-11. The difference in performance between the two electrocatalysts may be visualized in the N_2-derived CVs shown in Supplementary Fig. 23. In particular, the nature of the humps observed in the hydrogen adsorption and desorption regions (green-shaded region) under both half-cell (Supplementary Fig. 23a) and full-cell (Supplementary Fig. 23b) clearly shows that the adsorption on the PtMg/C-31 is significantly different from that of PtMg/C-11. This indicates that the exposed sites on the two electrocatalysts may be considerably different. In addition, the electrochemical surface area of PtMg/C-31 is substantially higher than that of PtMg/C-11. This is probably due to the higher exposed sites of Pt in the PtMg/C-31 in comparison to that of PtMg/C-11. Hence the difference in performance between the two electrocatalysts may be attributed to the relative composition of the catalyst, the exposed Pt sites, and the difference in ECSA. We also evaluated the performance of additional control samples, specifically, a PtMg alloy with a Pt to Mg precursor mass ratio of 2 to 1 (PtMg-21). Our findings reveal a consistent trend in stability akin to that observed

for PtMg/C-31 and PtMg/C-11. Notably the 4.5% drop in mass activity after 30k cycles underscores its stability under H_2-O_2 conditions (Supplementary Fig. 24). However, despite its stability, the mass activity at 0.9 V stands at 0.44 A mg_{Pt}^{-1} compared to the 0.50 A mg_{Pt}^{-1} recorded for PtMg/C-31. Furthermore, to emphasize the stability of the PtMg alloys is not solely attributable to the particle size effects, we synthesized Pt/C under identical synthesis conditions to PtMg/C except for the omission of Mg (Supplementary Fig. 25). The resulting polarization curves under H_2-O_2 and H_2-air conditions show values of 1340 and 630 mW cm^{-2} respectively, with a 15% degradation in peak power density after 30,000 cycles which are much lower than those found for PtMg/C-31. The TEM analyses (Supplementary Fig. 25c, d) show a transformation in the particle size of Pt/C-760 from 4.0 to 7.0 nm before and after ADT. These findings underscore the enhancement in both activity and stability conferred by Mg on Pt in PtMg alloys.

In addition to the electrochemical performance reported above, structural characterization conducted after the 30,000 ADT shows that the Pt/C particles increased from their initial average size of 1.8 nm to 4.0 nm, while that of the PtMg/C-31 increased from 5.8 to 6.0 nm (Supplementary Figs. 26 and 27). Significantly, the STEM and corresponding EDS elemental mapping images (Supplementary Figs. 28–30) of PtMg/C-31 NPs obtained before and after 30,000 ADT cycles show that the Pt and Mg are evenly distributed throughout the particles with an average Pt to Mg atomic ratio of 84: 16 after ADT, which represents a small decrease in Mg compared to the initial Pt to Mg average atomic ratio of 78 to 22. Furthermore, post-ADT XPS analysis in Supplementary Fig. 31 shows that the Pt4*f* doublets obtained after 30,000 cycles are shifted by 0.32 eV to higher binding energies relative to that initially recorded in Fig. 2b. We hypothesize that this shift in binding energy can be attributed to two factors; changes in the electronic structure of Pt atoms on the surface of the catalyst or the surface oxidation of Pt atoms. The change in the electronic structure of Pt could lead to a further downward alteration in the d-band center which would move the antibonding orbitals closer to the Fermi level. The binding energies are related to the energy required to remove an electron from a specific energy level in a material. Hence, as the Fermi-level moves closer to the antibonding states (energetically unfavorable state), the density of states (DOS) around the Fermi-level decreases, resulting in higher binding energy for the Pt 4*f* electrons. As the anti-bonding orbitals move closer to the Fermi level, it is expected that there would be a weak interaction between the Pt atoms and the various reaction intermediates (O*, OH*, OOH*). This probably accounts for the further positive shift in the CVs recorded in Supplementary Fig. 21. On the other hand, during the ADT cycles, some Mg leaches out of the nanoparticles (average concentration changes from ∽22 to ∽16%, Supplementary Figs. 28 and 29). Such a loss in Mg concentration could lead to a decreased interaction between Pt and Mg atoms, which would make the surface Pt atoms more susceptible to oxidation. It is not clear in our present study which of the two factors mentioned earlier contributes the most to the observed shift. However, we are certain the shift is a result of a combination of the aforementioned factors. A similar shift in binding energy was also observed for PtMg/C-11 after ADT (Supplementary Fig. 32). The activity and stability exhibited by the PtMg/C-31 cathode place it amongst the most competitive platinum-alkaline earth metal, platinum-rare earth metal, and platinum-early transition metal ORR catalysts reported to date (Supplementary Table 2). The activity and stability of this catalyst are also comparable to some platinum-transition metal catalysts measured under H_2-air conditions (Supplementary Table 3).

Computational results

DFT calculations were performed to elucidate the origin of the higher ORR activity and durability of PtMg NPs compared to Pt NPs. From the XRD and TEM data (Fig.1, Supplementary Fig. 2), the particles are mainly composed of $L1_2$ Pt_3Mg structures with a Pt-rich shell exposing (111) facets. Therefore, we use this structural model and refer to it as Pt_3Mg/Pt(111) in this section. A Bader charge analysis reveals charge transfer from Mg to Pt (≈ 0.54 e^- per Pt atom) leading to charge separation and stronger ionic bonding, resulting in compressive strain in the Pt_3Mg lattice as compared to Pt (0.37%, as shown in Fig. 5d which agrees with experiment; Supplementary Fig. 2). The LSV experiments in Fig. 3a show that Pt_3Mg has a higher on-set potential (lower overpotential) as compared to commercial Pt/C. To gain insight into the origin of the low overpotential, we considered the 4-step pathway mechanism for ORR considering the intermediates; OOH*, O*, OH* as shown in Fig. 5a. We constructed free energy diagrams at three different potentials U = 0 V, 1.23 V and at the onset potential. The onset potential is the lowest electrode potential at which all the reaction steps are downhill in the potential energy diagram (each step is exothermic). Our computational results from Fig. 5b, c show that the on-set potentials for Pt(111) and Pt_3Mg/Pt(111) are 0.66 and 0.73 V, respectively, indicating higher ORR activity for Pt_3Mg/Pt(111) which is in agreement with our experimental results. The higher on-set potential (lower overpotential) of Pt_3Mg is due to a combination of compressive strain and ligand effects resulting in weaker binding energies of OOH*, O* & OH* adsorbates compared to Pt. To further investigate the contributions of strain and ligand effects, we compared O* binding energy (where the optimal E_O is set to zero) on $Pt_3Mg/Pt_{1L}(111)$ vs strained Pt(111) as shown in Fig. 5d. In Fig. 5d, strained Pt monolayer (0.37% compressive strain) of $Pt_3Mg/Pt_{1L}(111)$ has an O binding energy of $\Delta E_O = -0.015$ eV which is higher than the $\Delta E_O = -0.17$ eV on Pt(111) slab with the same compressive strain. We can then infer that strain effects play a minor role and ligand effects are more important for the weak O binding on Pt_3Mg, which in turn is responsible for lower overpotential for ORR on Pt_3Mg.

Another key feature of the Pt_3Mg NPs is their high durability and their activity retention compared to commercial Pt/C. To understand the high durability, we have calculated Mg vacancy formation energies for Pt_3Mg/Pt(111) where a higher vacancy formation energy indicates it is thermodynamically less favorable to form the vacancy (more durable). In Fig. 5e, the Mg vacancy formation energies are shown for the different layers of Pt_3Mg which increases as Mg vacancies are formed from the inner layers (Mg_{vac}−1L = 2.72 eV, Mg_{vac}−2L = 3.04 eV, Mg_{vac}−3L = 3.17 eV). This indicates that it will be more difficult to remove Mg atoms from the Pt_3Mg once we have 1-2 monolayers of Pt covering Pt_3Mg NPs which agrees with our elemental mapping results from Fig. 2a. We subsequently compared the vacancy formation energy of Pt_3Mg with the other most stable forms of PtM alloys (M=Zn, Fe, Co, Ni) [values reported in J. Liang et al[4].] and plotted them against their corresponding formation energies in Fig. 5f. Since Pt_3Mg has higher vacancy formation energy compared to previously synthesized $L1_0$-PtMs, we can conclude that Pt_3Mg is more durable than other PtM alloy NPs. More DFT data are presented in Supplementary Figs. 33 and 34. In particular, the Pt vacancy formation energies presented in Supplementary Fig. 34 show that it is more difficult to create a vacancy on the Pt(111) surface of Pt_3Mg as compared to that of pure Pt. This can account for the lower surface oxidation and more durable ORR performance of PtMg/C-31 in comparison to that of commercial Pt/C (Fig. 2b).

Discussion

In summary, structurally ordered PtMg alloy catalysts in the form of NPs were successfully synthesized through the solution-phase approach for the first time. The particles were uniformly distributed on carbon support with an average particle size of 5.76 nm. Further studies disclosed that the PtMg alloy exhibited compressive strains along two crystallographic directions and ligand effects between the intermetallic core and the Pt-rich shell. As a result, in the

https://doi.org/10.1038/s41467-024-51280-2

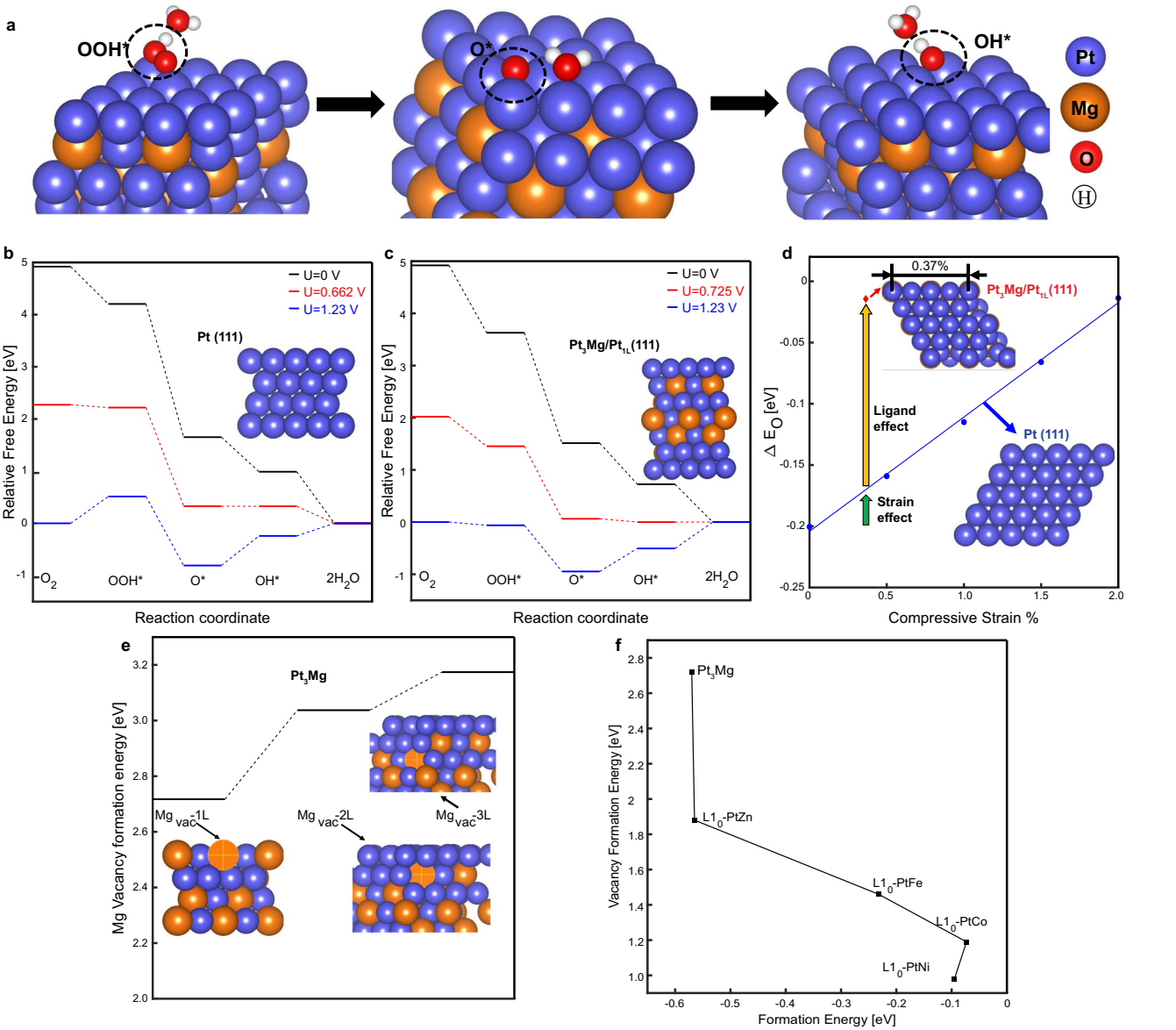

Fig. 5 | DFT Calculations. a ORR 4-step pathway for the different intermediates on $Pt_3Mg/Pt_{1L}(111)$. ORR free energy diagrams for **b** Pt(111), **c** $Pt_3Mg/Pt_{1L}(111)$, **d** ΔE_O vs compressive strain of (111) surface, where $\Delta E_O = E_O - E_{O_{optimal}}$, **e** Mg vacancy formation energies for Mg atoms from the surface (1L) and sub-surface (2 L and 3 L) layers of $Pt_3Mg(111)$, **f** Correlation between vacancy formation energies and formation energies for Pt_3Mg vs previously reported $L1_0$-PtM systems[4].

half-cell RDE test, the as-synthesized catalysts exhibited improvement in activity and stability over the commercial Pt/C catalyst, displaying negligible decay over 30,000 cycles. Furthermore, when the PtMg/C samples were employed as cathode catalysts in PEMFC, the PtMg/C-31 in particular displayed initial power densities of 1575 and 850 mW cm^{-2} under H_2-O_2 and H_2-air conditions, respectively. After 30,000 durability test cycles, only a 6 and 5% drop in power densities were recorded under the aforementioned conditions, respectively. DFT calculations explain that the stability observed in this alloy system exudes from the high vacancy formation energy of Mg which is about two-fold that of highly active and stable Pt-transition metal alloys, while the ligand and strain effects contribute to the activity. This study opens up new opportunity to further extend the Pt alloy region to the area with alkaline earth metals in the form of nanoparticles; an area which has been rarely explored due to the difficulty in synthesis. This work also lays the foundation for the future development of stable electrocatalysts for energy applications.

Methods

Chemicals and materials

Acetic acid, platinum (IV) chloride ($PtCl_4$, ≥ 99.9%), magnesium chloride ($MgCl_2$ > 98%), calcium chloride ($CaCl_2$, ≥ 97.0%), yttrium (III) chloride (YCl_3 > 99.9%), strontium chloride ($SrCl_2$ > 99.9%), barium chloride ($BaCl_2$ > 99.9%), sodium borohydride ($NaBH_4$ > 98.0%), potassium triethylborohydride (KEt_3BH), lithium triethylborohydride ($LiEt_3BH$), ascorbic acid ($C_6H_8O_6$), glucose ($C_6H_{12}O_6$, ≥ 99.5%), phloroglucinol ($C_6H_6O_3$, ≥ 99.0%), N-N dimethylformamide (DMF), and 5 wt% Nafion ionomer solution were all purchased from Sigma-Aldrich Korea. Pt-solution (100 mg/ml) was purchased from Korea, the magnesium powder from Alfa Aesar Korea, the commercial Pt/C (20wt% Pt, TEC10E20E, E-type carbon, BET surface area 565.8 m^2/g_{cat}) from Tanaka Kikinzoku Kogyo, Japan, vulcan carbon (Vulcan XC72) from Cobot, and commercial carbon (Ketjen Black EC300JD, BET surface area 885 m^2g^{-1}) from Ketjen Black international. All chemicals were used as received without further treatment and all water used in the experiment was made by passing through an ultrapure purification system.

Synthesis

PtMg/C NPs were prepared through three systematic steps of I) solvolysis, II) alloying and atomic ordering, and III) creation of Pt skin. Before the synthesis, an excess amount of N, N-dimethylformamide (DMF) was degassed at 120 °C using a two-necked flask connected to a vacuum line. After degassing, nitrogen gas (N_2) was bubbled through the solvent for 30 min to drive out any remaining oxygen residue, and the resulting DMF was stored in an argon-filled glove box. In a typical synthesis, 25.0 mg of platinum (IV) chloride ($PtCl_4$), 9.0 to 75.0 mg of magnesium chloride ($MgCl_2$), and 18.0 mg of sodium borohydride ($NaBH_4$) were dissolved into 15 mL pre-degassed DMF aprotic solvent in a vial under inert conditions in an argon-filled glove box. After the vial was capped and sealed with Teflon tape, the mixture was ultrasonicated for 2 h. The resulting mixture was transferred into a Teflon-lined autoclave (25 mL) and heated from room temperature to 165 °C. The temperature was maintained at 165 °C for 12 h. The reaction mixture was allowed to naturally cool to room temperature, mixed with 100 mg of high surface area carbon (Ketjen Black EC 300 J), sonicated for 2 h, and stirred further for 3 h under an Ar atmosphere. The obtained catalyst was dried in a vacuum and mixed with a small amount of powdered potassium triethylborohydride (KEt_3BH). All the experimental steps have been done under the inert gas condition. Subsequently, heat treatment was performed in NH_3 gas from room temperature to 180 °C and maintained at that temperature for 30 minutes, followed by flowing excess 5% H_2/Ar to 760 °C for 2 h at a ramp rate of 10 °C min^{-1} to get ordered PtMg alloy structure. Finally, acid etching of the PtMg/C samples was completed in 0.5 M acetic acid for 12 h at 60 °C to remove impurities on the surface along with the Pt-rich shell formation on the PtMg surface. The final product was collected for further characterization.

Characterization

Transmission electron microscopy (TEM) was taken from a Hitachi HF-3300 attached to a dual-beam focused ion beam Hitachi-NB-5000. Thermis Z with NTIS number NFEC-2019-05-255960 was used for high-resolution TEM (HR-TEM), ultra-high-resolution transmission electron microscopy (UHRTEM), scanning transmission electron microscopy (STEM) analysis and energy dispersive X-ray spectroscopy (EDS) elemental mapping. The particle size distribution was analyzed using the ImageJ software. PXRD patterns were collected using a Rigaku Smartlab diffractometer with Cu-Kα (0.15406 nm). The operation voltage, current, resolution, and scan rate were 40 kV, 30 mA, 0.020, and 4° min^{-1} respectively. X-ray photoelectron spectroscopy (XPS) was conducted using a Thermoscientific ESCALAB 250Xi. The XPS spectra were deconvoluted using the CASA XPS software and fitted using the curve fitting program; OriginPro 2017. X-ray absorption near edge structure (XANES) and extended X-ray absorption fine structure (EXAFS) at the Pt *L*3-edge were performed at the synchrotron center in Korea; Pohang Accelerator Laboratory with beamline number 8 C. The electron-storage ring operates in a voltage range of 4.0 ∽ 22.0 keV using Si (111) mode. All the XAS data were recorded at room temperature using the Transmittance mode. The XANES and EXAFS spectra were fitted using the Athena and Artemis software packages and plotted via the Origin software.

Electrochemical measurements

All electrochemical measurements were conducted in a three-electrode cell using the rotating disk electrode (RDE) connected to an electrochemical analyzer (Biologic VMP3) at room temperature. Glassy carbon was used as the working electrode with a diameter of 3 mm. The glassy carbon was coated with the as-synthesized catalyst or commercial Pt/C in all measurements. In short, the catalyst ink was prepared by dispersing 2.5 mg of catalyst powders in 4 mL of deionized water (D.I water), 0.95 mL of isopropanol (IPA), and 0.5 mL of 5 wt% Nafion solution. The resulting solution was sonicated for 1 hour to form a uniform slurry. Subsequently, 1.5 μL of the slurry was drop cast over the working electrode and dried under ambient conditions. Pt wire was used as the counter electrode and Ag/AgCl with saturated KCl as the reference electrode to complete the three-electrode cell. All measurements were conducted in a 0.1 M $HClO_4$ solution. Oxygen reduction reaction (ORR) measurements were achieved by saturating the 0.1 M $HClO_4$ solution with oxygen at a scan rate of 10 mV/s and a working electrode rotation speed of 1600 rpm. The accelerated degradation tests (ADT) were performed at room temperature in N_2-saturated 0.1 M $HClO_4$ by applying cyclic potential sweeps between 0.60 and 0.95 V versus the reversible hydrogen electrode (RHE) at a sweep rate of 100 mV/s for 10k, 20k, and 30k cycles, after which LSV curves were measured for each successive cycle. The electrochemical active surface area (ECSA) measurements were determined by integrating the hydrogen desorption charge on cyclic voltammetry (CV) at room temperature in N_2-saturated 0.1 M $HClO_4$. The ECSA is calculated using the following equation;

$$ECSA_{Ptcat}\left(\frac{m^2}{g_{Pt}}\right) = \left[\frac{Q_{H-desorption}(C)}{210\mu C/cm^2\, X\, L_{pt}\left(\frac{mg_{pt}}{cm^2}\right)A_g}\right] X10^5 \quad (1)$$

Where $Q_{H\text{-adsorption}}$ is the hydrogen desorption charge obtained by integrating the area in the CVs. 210 is the charge of a monolayer. L_{Pt} represents the catalyst loading on the electrode surface. A_g is the geometric surface area of the glassy carbon electrode (i.e., 0.071 cm^2). The kinetic currents were obtained by employing the Koutecky-Levich equation:

$$j_k = \frac{j\, X\, j_d}{j_d - j} \quad (2)$$

where j_k represents the kinetic current density, j is the current density obtained from LSV measurements and j_d is the diffusion-limited current density. The mass activity (MA) of each catalyst was obtained using the equation

$$MA = \frac{j_k}{Lpt} \quad (3)$$

specific activities were calculated from the MAs by normalizing with the ECSA.

MEA preparation and fuel cell test

The catalysts (Pt/C or PtMg/C) were mixed with a 5 wt% Nafion ionomer solution, isopropanol, and D.I water by ultrasonication for 1 hour to form a homogeneous ink. The catalyst slurries were then spray-coated on a Nafion 211 membrane (Dupont). In all PEMFC performance tests, commercial Pt/C (TKK, 19.4 wt% Pt) was used as the anode catalyst, and the electrode area for both the anode and cathode was maintained at 5 cm^2. PtMg/C was employed as a cathode catalyst. The anode catalyst loadings were maintained at 0.05 mg_{Pt} cm^{-2} while the cathode catalyst loadings were 0.10 and 0.080 mg_{Pt} cm^{-2} for Pt/C and PtMg/C-31, respectively. The membrane electrode assemblies (MEAs) were assembled with commercial gas diffusion layers (GDL, SGL 39 BC) without hot-pressing. MEAs were prepared by using catalyst-coated membranes (CCMs). The cell was operated at 80 °C with a back pressure of 0.5 bar. Pure hydrogen and oxygen with 100% relative humidity (RH) were supplied to the anode and cathode at flow rates of 300 mL/min and 1000 mL/min, respectively. In H_2-air measurements, pure O_2 was substituted for atmospheric air. Fuel cell polarization curves were recorded using a PEMFC test station (Scitech Inc., KOREA) with an electronic load (PLZ664 WA, Kikusui). The accelerated durability test (ADT) was conducted by

applying cyclic sweeps from 0.60 to 0.95 V with 3 s hold-time at both potentials and a rise time of 0.5 s according to US DOE protocol[57]. Polarization curves and electrochemical impedance spectroscopy (EIS) (@100 mA/cm^2) were recorded at the start and after 10k, 20k, and 30k cycles of the durability testing protocol. All polarization curves reported are without an iR correction. The mass activity was determined at 0.9 V based on the Pt loading amount.

Computational details

All density functional theory (DFT) calculations were based on the generalized gradient approximation and projector augmented wave methods which were performed using the Vienna Ab initio Simulation Package[58–62]. Kohn-Sham wave functions were expanded in a plane wave basis set with an energy cutoff of 420 eV using a Gaussian smearing width of 0.05 eV[63]. The Perdew-Burke-Ernzerhof function was used to describe the electron exchange and correlation[64]. The Brillouin zone was sampled using a $(2\times2\times1)$ Monkhorst-Pack mesh[65]. The convergence criteria for electronic and geometric optimization were 10^{-6} eV and 0.01 eV Å^{-1}, respectively. To account for solvation effects, we included hybrid solvation with both implicit and explicit solvation. Implicit solvation is considered using the VASPsol package[66,67] by setting the dielectric constant to 78.4 to represent water and explicit solvation is considered by having a water molecule near an intermediate. By using the hybrid solvation model, we have accounted for hydrogen bonding which is important to get the accurate binding energies of ORR intermediates the calculations are also a lot cheaper than the ones with only explicit solvation. The catalytic reactions on the alloy nanoparticle surfaces were modeled using p(4 × 4) four-layer (Pt) and seven-layer (Pt_3Mg) *fcc* {111} slabs with 12 Å of vacuum along the *z*-direction to separate the periodic images of the slab and minimize their interactions. The bottom two layers were constrained to bulk lattice parameters, and the top layers were unconstrained to mimic the NP surface. Free energy diagrams were constructed by calculating the binding energies (E_b) of various adsorbate species (e.g., OOH, O, OH etc.) at different alloy sites using Eq. 4,

$$\mathrm{E_b} = \mathrm{E_{total}} - \mathrm{E_{slab}} - \mathrm{E_{adsorbate}} + \mathrm{ZPE} \tag{4}$$

where E_{total} is the total energy of the adsorption system (*i.e.*, the slab with the adsorbate attached), E_{slab} is the total energy of the bare slab, $E_{adsorbate}$ is the total energy of the adsorbate in a vacuum and ZPE is zero-point energy corrections. All the reaction steps for the ORR are shown in the following Eq. (5),

$$\begin{aligned} O_2(g) + 4H^+ + 4e^- + * \rightarrow OOH^* + 3H^+ + 3e^- \rightarrow O^* + 2H^+ + 2e^- + H_2O(l) \\ \rightarrow OH^* + H^+ + e^- + H_2O(l) \rightarrow 2H_2O(l) \end{aligned} \tag{5}$$

The free energies (eV) of each step were calculated as follows

$$G_1(U) = 4.92 - 4\times U \tag{6}$$

$$G_2(U) = E_{OOH^*,b} + 1.5\times E_{H_2} - 2\times E_{H_2O} - 3\times U \tag{7}$$

$$G_3(U) = E_{O^*,b} + E_{H_2} - E_{H_2O} - 2\times U \tag{8}$$

$$G_4(U) = E_{OH^*,b} + 0.5\times E_{H_2} - E_{H_2O} - 1\times U \tag{9}$$

$$G_5(U) = 0 \tag{10}$$

where U is applied potential (V) and $E_{X^*,b}$ is the binding energy of a species X.

Data availability

All data that support the findings of this study are available in the main text, figures, and Supplementary Information. Source data are provided with this paper.

References

1. Jiao, Y., Zheng, Y., Jaroniec, M. & Qiao, S. Z. Design of electrocatalysts for oxygen- and hydrogen-involving energy conversion reactions. *Chem. Soc. Rev.* **44**, 2060–2086 (2015).
2. Lee, H.-Y. et al. Low temperature synthesis of new highly graphitized N-doped carbon for Pt fuel cell supports, satisfying DOE 2025 durability standards for both catalyst and support. *Appl. Catal. B Environ.* **323**, 122179 (2023).
3. Debe, M. K. Electrocatalyst approaches and challenges for automotive fuel cells. *Nature* **486**, 43–51 (2012).
4. Liang, J. et al. Biaxial strains mediated oxygen reduction electrocatalysis on Fenton reaction resistant $L1_0$ -PtZn fuel cell cathode. *Adv. Energy Mater.* **10**, 2000179 (2020).
5. Tilley, R. D. & Gooding, J. J. Electrocatalysis: understanding platinum migration. *Nat. Energy 2016 111* **1**, 1–2 (2016).
6. Ooka, H., Huang, J. & Exner, K. S. The Sabatier principle in electrocatalysis: basics, limitations, and extensions. *Front. Energy Res.* **9**, 155 (2021).
7. Greeley, J. et al. Alloys of platinum and early transition metals as oxygen reduction electrocatalysts. *Nat. Chem.* **1**, 552–556 (2009).
8. Cui, Z. et al. Synthesis of structurally ordered Pt_3Ti and Pt_3V nanoparticles as methanol oxidation catalysts. *J. Am. Chem. Soc.* **136**, 10206–10209 (2014).
9. Tetteh, E. B. et al. Strained Pt(221) facet in a PtCo@Pt-Rich catalyst boosts oxygen reduction and hydrogen evolution activity. *ACS Appl. Mater. Interfaces* **14**, 25246–25256 (2022).
10. Li, J. et al. Hard-magnet $L1_0$-CoPt nanoparticles advance fuel cell catalysis. *Joule* **3**, 124–135 (2019).
11. Yang, C.-L. et al. Sulfur-anchoring synthesis of platinum intermetallic nanoparticle catalysts for fuel cells. *Science* **374**, 459–464 (2021).
12. Xiao, F. et al. Atomically dispersed Pt and Fe sites and Pt–Fe nanoparticles for durable proton exchange membrane fuel cells. *Nat. Catal. 2022 56* **5**, 503–512 (2022).
13. Tian, X. et al. Engineering bunched Pt-Ni alloy nanocages for efficient oxygen reduction in practical fuel cells. *Science* **366**, 850–856 (2019).
14. Niu, G. et al. Synthesis of Pt-Ni octahedra in continuous-flow droplet reactors for the scalable production of highly active catalysts toward oxygen reduction. *Nano Lett.* **16**, 3850–3857 (2016).
15. Hu, Y., Jensen, J. O., Cleemann, L. N., Brandes, B. A. & Li, Q. Synthesis of Pt-rare earth metal nanoalloys. *J. Am. Chem. Soc.* **142**, 953–961 (2020).
16. Escudero-Escribano, M. et al. Pt_5Gd as a highly active and stable catalyst for oxygen electroreduction. *J. Am. Chem. Soc.* **134**, 16476–16479 (2012).
17. Malacrida, P., Escudero-Escribano, M., Verdaguer-Casadevall, A., Stephens, I. E. L. & Chorkendorff, I. Enhanced activity and stability of Pt-La and Pt-Ce alloys for oxygen electroreduction: The elucidation of the active surface phase. *J. Mater. Chem. A* **2**, 4234–4243 (2014).
18. Yoo, S. J. et al. Enhanced stability and activity of Pt-Y alloy catalysts for electrocatalytic oxygen reduction. *Chem. Commun.* **47**, 11414–11416 (2011).
19. Hernandez-Fernandez, P. et al. Mass-selected nanoparticles of Pt_xY as model catalysts for oxygen electroreduction. *Nat. Chem* **6**, 732–738 (2014).
20. Stephens, I. E. L., Bondarenko, A. S., Grønbjerg, U., Rossmeisl, J. & Chorkendorff, I. Understanding the electrocatalysis of oxygen reduction on platinum and its alloys. *Energy Environ. Sci.* **5**, 6744–6762 (2012).

21. Yoo, S. J. et al. Promoting effects of La for improved oxygen reduction activity and high stability of Pt on Pt-La alloy electrodes. *Energy Environ. Sci.* **5**, 7521–7525 (2012).
22. Chen, Y. et al. A highly efficient multi-phase catalyst dramatically enhances the rate of oxygen reduction. *Joule* **2**, 938–949 (2018).
23. Tian, X., Lu, X. F., Xia, B. Y. & Lou, X. W. D. Advanced electrocatalysts for the oxygen reduction reaction in energy conversion technologies. *Joule* **4**, 45–68 (2020).
24. Itahara, H. et al. Eutectic salt mixture-assisted sodium-vapor-induced synthesis of Pt–Ca nanoparticles, and their microstructural and electrocatalytic properties. *Chem. Commun.* **57**, 4279–4282 (2021).
25. Liu, X. et al. Ultrasmall Pt_2Sr alloy nanoparticles as efficient bifunctional electrocatalysts for oxygen reduction and hydrogen evolution in acidic media. *J. Energy Chem.* **64**, 315–322 (2022).
26. Agnarelli, L. et al. Mg_3Pt_2: Anionic chains in a Eu_3Ga_2-type structure. *Inorg. Chem.* **60**, 13681–13690 (2021).
27. Xia, W., Mahmood, A., Liang, Z., Zou, R. & Guo, S. Earth-abundant nanomaterials for oxygen reduction. *Angew. Chemie Int. Ed* **55**, 2650–2676 (2016).
28. Tetteh, E. B. et al. New PtMg Alloy with durable electrocatalytic performance for oxygen reduction reaction in proton exchange membrane fuel cell. *ACS Energy Lett.* **5**, 1601–1609 (2020).
29. Stamenkovic, V. R. et al. Trends in electrocatalysis on extended and nanoscale Pt-bimetallic alloy surfaces. *Nat. Mater.* **6**, 241–247 (2007).
30. Jinnouchi, R., Toyoda, E., Hatanaka, T. & Morimoto, Y. First principles calculations on site-dependent dissolution potentials of supported and unsupported Pt particles. *J. Phys. Chem. C* **114**, 17557–17568 (2010).
31. Shin, C.-H., Lee, H.-Y., Gyan-Barimah, C., Yu, J.-H. & Yu, J.-S. Magnesium: properties and rich chemistry for new material synthesis and energy applications. *Chem. Soc. Rev.* **52**, 2145–2192 (2023).
32. Stadelmaier, H. H. & Hardy, W. K. Ternäre Kohlenstofllegierungen von Palladium und Platın mit Magnesium, Aluminium, Zink, Gallium, Germanium, Kadmium, Indium, Zinn, Quecksilber, Thallıum und Blei. *Int. J. Mater. Res.* **52**, 391–396 (1961).
33. Linsinger, S. et al. Intermetallic magnesium compounds $RE_2Ni_2Mg_3$ (RE =Gd, Dy-Tm, Lu) with $Tb_2Ni_2Mg_3$-type structure. *Zeitschrift fur Naturforsch. B J. Chem. Sci.* **65**, 1305–1310 (2010).
34. Escudero-Escribano, M. et al. Tuning the activity of Pt alloy electrocatalysts by means of the lanthanide contraction. *Science* **352**, 73–76 (2016).
35. Du, X. X., He, Y., Wang, X. X. & Wang, J. N. Fine-grained and fully ordered intermetallic PtFe catalysts with largely enhanced catalytic activity and durability. *Energy Environ. Sci.* **9**, 2623–2632 (2016).
36. Luo, M. & Guo, S. Strain-controlled electrocatalysis on multimetallic nanomaterials. *Nat. Rev. Mater.* **2**, 17059 (2017).
37. Stamenkovic, V. et al. Changing the activity of electrocatalysts for oxygen reduction by tuning the surface electronic structure. *Angew. Chem. Int. Ed.* **45**, 2897–2901 (2006).
38. Fichtner, J. et al. Top-down synthesis of nanostructured platinum-lanthanide alloy oxygen reduction reaction catalysts: Pt_xPr/C as an example. *ACS Appl. Mater. Interfaces* **11**, 5129–5135 (2019).
39. Kobayashi, Y., Tada, S. & Kikuchi, R. Simple chemical synthesis of intermetallic Pt_2 Y bulk nanopowder. *Mater. Adv.* **1**, 2202–2205 (2020).
40. Salvador, J. R., Herbst, J. F. & Meyer, M. S. Synthesis and hydriding behavior of Li_2MgPt. *J. Alloys Compd.* **509**, 2650–2653 (2011).
41. Aleandri, L., Bogdanović, B., Wilczok, U., Noréus, D. & Block, G. Low temperature synthesis and structural characterization of three novel magnesium platinum intermetallics, t-$MgPtC_xH_y$, t-$Mg_2PtC_xH_y$, m-Mg_2PtC_xHy. *Zeitschrift fur. Phys. Chemie* **185**, 131–144 (1994).
42. Range, K. J. & Hafner, P. A redetermination of the crystal structure of trimagnesium platinum, Mg_3Pt. *J. Alloys Compd.* **183**, 430–437 (1992).
43. Zhang, S. et al. Rare-earth incorporated alloy catalysts: synthesis, properties, and applications. *Adv. Mater.* **33**, 2005988 (2021).
44. Li, Q. et al. New approach to fully ordered fct-FePt nanoparticles for much enhanced electrocatalysis in acid. *Nano Lett* **15**, 2468–2473 (2015).
45. Kim, J., Lee, Y. & Sun, S. Structurally ordered FePt nanoparticles and their enhanced catalysis for oxygen reduction reaction. *J. Am. Chem. Soc.* **132**, 4996–4997 (2010).
46. Cheng, X. et al. Nano-geometric deformation and synergistic Co nanoparticles—Co-N_4 composite sites for proton exchange membrane fuel cells. *Energy Environ. Sci.* **14**, 5958–5967 (2021).
47. Liang, J. et al. Tungsten-doped $L1_0$-PtCo ultrasmall nanoparticles as a high-performance fuel cell cathode. *Angew. Chemie Int. Ed* **58**, 15471–15477 (2019).
48. Wei, X. et al. Synergistically enhanced single-atomic site Fe by Fe_3C@C for boosted oxygen reduction in neutral electrolyte. *Nano Energy* **84**, 105840 (2021).
49. Albrecht, A. et al. Nitriding and denitriding of nanocrystalline iron system with bimodal crystallite size distribution. *Mater.* **15**, 143 (2021).
50. Bu, L. et al. PtPb/PtNi Intermetallic core/atomic layer shell octahedra for efficient oxygen reduction electrocatalysis. *J. Am. Chem. Soc.* **139**, 9576–9582 (2017).
51. Bu, L. et al. Biaxially strained PtPb/Pt core/shell nanoplate boosts oxygen reduction catalysis. *Science* **354**, 1410–1414 (2016).
52. Mukerjee, S. Role of structural and electronic properties of Pt and Pt Alloys on electrocatalysis of oxygen reduction. *J. Electrochem. Soc.* **142**, 1409 (1995).
53. Choi, D. S., Robertson, A. W., Warner, J. H., Kim, S. O. & Kim, H. Low-temperature chemical vapor deposition synthesis of Pt-Co alloyed nanoparticles with enhanced oxygen reduction reaction catalysis. *Adv. Mater.* **28**, 7115–7122 (2016).
54. Liu, M. et al. Concave Pt–Zn nanocubes with high-index faceted Pt Skin as highly efficient oxygen reduction catalyst. *Adv. Sci.* **9**, 2200147 (2022).
55. Allen, J., Bard, Larry, R., Faulkner, Henry, S. *Electrochemical Methods: Fundamentals and Applications* (Wiley, 2000).
56. US Department of Energy. https://www.energy.gov/eere/fuelcells/doe-technical-targets-polymer-electrolyte-membrane-fuel-cell-components (2018).
57. US Department of Energy. The Fuel Cell Technologies office multi-year research, development, and demonstration plan. (*US Department of Energy, 2016*).
58. Kresse, G. & Hafner, J. Ab initio molecular dynamics for open-shell transition metals. *Phys. Rev. B* **48**, 13115–13118 (1993).
59. Kresse, G. & Hafner, J. Ab initio molecular-dynamics simulation of the liquid-metal–amorphous-semiconductor transition in germanium. *Phys. Rev. B* **49**, 14251 (1994).
60. Kresse, G. & Furthmüller, J. Efficiency of ab-initio total energy calculations for metals and semiconductors using a plane-wave basis set. *Comput. Mater. Sci.* **6**, 15–50 (1996).
61. Kresse, G. & Furthmüller, J. Efficient iterative schemes for ab initio total-energy calculations using a plane-wave basis set. *Phys. Rev. B - Condens. Matter Mater. Phys.* **54**, 11169–11186 (1996).
62. Joubert, D. From ultrasoft pseudopotentials to the projector augmented-wave method. *Phys. Rev. B Condens. Matter Mater. Phys.* **59**, 1758–1775 (1999).
63. Kohn, W. & Sham, L. J. Self-consistent equations including exchange and correlation effects. *Phys. Rev.* **140**, A1133 (1965).
64. Perdew, J. P., Burke, K. & Ernzerhof, M. Generalized gradient approximation made simple. *Phys. Rev. Lett.* **77**, 3865 (1996).
65. Monkhorst, H. J. & Pack, J. D. Special points for Brillouin-zone integrations. *Phys. Rev. B* **13**, 5188–5192 (1976).

66. Mathew, K., Sundararaman, R., Letchworth-Weaver, K., Arias, T. A. & Hennig, R. G. Implicit solvation model for density-functional study of nanocrystal surfaces and reaction pathways. *J. Chem. Phys.* **140**, 84106 (2014).
67. Mathew, K., Kolluru, V. S. C., Mula, S., Steinmann, S. N. & Hennig, R. G. Implicit self-consistent electrolyte model in plane-wave density-functional theory. *J. Chem. Phys.* **151**, 234101 (2019).

Acknowledgements

This work was generously supported by National Research Foundation (NRF) grants (RS-2024-00345686-JSY and RS-2023-00223196-JSY) funded by the Korean government. The authors would like to thank the Korean Basic Science Institute (KBSI) at Jeonju and Daejon as well as the Center for Core Research Facilities (CCRF) in DGIST.

Author contributions

Conceptualization: C.G.B. and J.S.Y.; methodology: C.G.B.; investigation: C.G.B., L.H.Y., J.S.Y.; visualization: C.G.B., L.H.Y., Y.W., C.H.S., M.I.M., J.K.K.; funding acquisition and project administration: J.S.Y.; theoretical study: J.S.P.M. and G.H.; supervision: J.S.Y. and G.H.; writing – original draft: C.G.B., J.S.Y., J.S.P.M.; Writing – review & editing: C.G.B., J.S.P.M., L.H.Y., Y.W., C.H.S., M.I.M., J.K.K., G.H., J.S.Y.

Competing interests

The authors declare no competing interests.

Additional information

Supplementary information The online version contains supplementary material available at https://doi.org/10.1038/s41467-024-51280-2.

Correspondence and requests for materials should be addressed to Graeme Henkelman or Jong-Sung Yu.

Peer review information *Nature Communications* thanks the anonymous reviewers for their contribution to the peer review of this work. A peer review file is available.